

RESEARCH ARTICLE

Laminar-turbulent transition detection on airfoils by high-frequency microphone measurements

Özge Sinem Özçakmak¹  | Niels Nørmark Sørensen¹  | Helge Aagaard Madsen¹  |
Jens Nørkær Sørensen² 

¹Department of Wind Energy, Technical University of Denmark, Roskilde, Denmark

²Department of Wind Energy, Technical University of Denmark, Lyngby, Denmark

Correspondence

Özge Sinem Özçakmak, Department of Wind Energy, Technical University of Denmark, Roskilde, Denmark.
Email: ozsi@dtu.dk

Present Address

DTU Wind Energy Frederiksborgvej 399 DTU Vind Building: 125, S40 Roskilde, 4000 Denmark

Funding information

Danmarks Tekniske Universitet

Abstract

In the present work, various data processing methods for laminar to turbulent transition detection on airfoils are assessed based on experimental data. For this purpose, NACA 63-418 airfoil profile with surface microphones flush mounted both on the suction and the pressure side is used in the wind tunnel experiments. Reynolds numbers are changed in the range from $1.6 \cdot 10^6$ to $6 \cdot 10^6$ for various angles of attack. In this way, the transition behaviour of the airfoil is characterized. Time signals and spectrogram of the data, chordwise pressure level changes, and first moments are investigated. Standard deviations of pressure are observed to exhibit a peak at transition and slightly decreases for the fully turbulent flow staying always higher than the laminar flow. The most robust method to detect the transition location is found to be the characteristic frequency approach by spectral moments provided that the inflow turbulence is low. The numerical results are in agreement with experimental results on the pressure side where natural transition occurs. However, the transition due to surface irregularity and microphone placement occurs on the suction side. This cannot be predicted by the numerical tools. The Tollmien-Schlichting wave frequencies and neutral curve points are determined from the experiments. The analysis shows that the most common curve length of the transition process is around 15% to 20%, and it can vary between 0% to 30 % of the chord. Increasing the Reynolds number leads to an earlier transition position closer to leading edge at both upper and lower surfaces.

KEYWORDS

boundary layer, laminar-turbulent transition, transition detection, wind tunnel experiments, wind turbine airfoil

1 | INTRODUCTION

As the size of modern wind turbines is steadily growing, high Reynolds number experimental data for the wind turbine airfoils and blades are needed for verification and improvement of the aerodynamic prediction tools in the design process. In order to contribute to the development of the airfoil design and to accurately predict airfoil characteristics, the determination of the laminar-turbulent transition point is very important.¹ Power curves, which are the indication of the electrical power output at different incoming wind speeds, are highly affected by the lift to drag ratio of the aerodynamic profiles of wind turbines. However, the maximum lift coefficient must be limited due to structural load constraints, which makes drag force one of the major parameters to be studied.² Skin friction drag of a laminar boundary layer is significantly lower than that of a turbulent boundary layer. Therefore, by the detection of the transition location from laminar to turbulent flow, it is possible to have an improved frictional drag estimation. Moreover, transition location control mechanisms can be applied to obtain higher lift to drag ratio airfoils.

It was hypothesized by Reynolds that the transition is a result of instabilities in the laminar flow, which was further developed by Rayleigh.³ On a given body, starting from a laminar flow, the transition process is characterized by three successive steps of receptivity, linear instability, and non-linear instability, which ultimately leads to turbulent flow.⁴ In the receptivity region, disturbances like Tollmien-Schlichting (T-S) waves, crossflow perturbations, and streaks can be triggered inside the laminar boundary layer by free stream turbulence, pressure velocity

fluctuations, surface roughness and irregularities, etc. In the second step, the unstable waves described by linear stability theory go through a linear amplification.⁵ As the amplitude grows and the unstable waves reach to a finite amplitude, non-linear interactions in the form of secondary instabilities are seen at the third step of the transition process.⁶ Disturbance growth becomes very rapid in this step resulting in turbulence. Later, these theories were extended by including the effect of other parameters on the transition (pressure gradient, suction, Mach number, heat transfer) by using the stability theory of the boundary layer.⁷ On the other hand, in many other cases, where there are flow disturbances such as high free stream turbulence and large surface roughness and irregularities, the transition can occur in the absence of T-S waves. In those cases, the flow does not go through a gradual process. The growth of two dimensional waves and their secondary instability are bypassed and the disturbances develop directly into turbulence.^{8,9} This transition process is called "bypass transition" by Morkovin.¹⁰

For many years, experimental studies have been devoted to laminar-turbulent transition, to understand in detail the transition process and to generate transition detection databases for computational validations and improvements. Some of the most common experimental methods are using pressure transducers,¹¹ hot film sensors,¹²⁻¹⁴ and infrared thermography.^{15,16} Although there are many experiments conducted in literature for detection of the laminar-turbulent transition in aircraft applications, research on wind turbine blades are comparably rare. There is a need for characterization of transition on wind turbine blades for high Reynolds number flows.

Large experimental datasets obtained from the DAN-AERO Experiments¹⁷⁻¹⁹ are processed, and a database based on these measurements is generated. The transition from laminar to turbulent flow is noticeable by a great increase in the boundary layer thickness, the wall shear stress, wall heat flux, and the fluctuations of the wall static pressure.⁷ Therefore, pressure fluctuations on the airfoil surface were measured by surface flush-mounted microphones that have a high-frequency response. Having sufficient amount of microphones along the chord, an autonomous data processing method to detect transition is built. Time data and power spectral density (PSD) analysis are performed for surface pressure readings from microphones in order to detect the transition location on the airfoil. Pressure levels (Lps) and moment of the spectra are analysed for various Reynolds numbers and angle of attack (AOA) values. The growth of the initial disturbances and transition locations are presented.

2 | EXPERIMENTAL PROCEDURE AND SET-UP

The wind tunnel experiments were conducted on a 2-D wing model equipped with surface flush-mounted microphones in order to investigate the correlation between boundary layer transition and surface pressure spectra. Although NACA 4 and 5 series are not preferred anymore by the wind turbine industry due to airfoils' sensitivity to roughness, NACA 63 and 64 six-digit series are still in use in wind turbine blades.²⁰ The NACA 63-418 airfoil profile was used in the wind turbine industry due to its smooth stall characteristics and its relatively high insensitivity of the maximum lift to leading edge roughness with good structural characteristics.¹⁸ The airfoil used in the experiments is manufactured identically to the most outward section (37 meters far from the hub) of the LM 38.8 blade of the NM80 wind turbine and has therefore the same surface irregularities as the full scale blade. The chord of the manufactured model is 0.9 m. The theoretical NACA 63-418 airfoil profile and the contour measured on the experimental model with microphone placement are shown in Figure 1. Pressure taps are also installed on the model. The spanwise distribution of the microphones and the pressure taps for the 3-D blade are presented at Figure 2. The same distribution is applied to the wind tunnel model by scaling down the chord from 1.2 to 0.9 m and shifting some of the leading edge microphones in spanwise direction during installation.

Excluding the broken sensors, 35 high-frequency microphones on the suction side and 21 on the pressure side are used for the analysis. The microphones have a diameter of around 4 mm and are installed about 1 mm below the surface of the airfoil via pinhole. The pinhole has a diameter of 1 mm, which is the effective wetted measurement area. The NM80 wind turbine, the manufactured wing model, and the installed microphones are shown in Figure 3. As it can be seen from the figure, microphones are also distributed in the spanwise direction in order to reduce disturbances from upstream microphones.

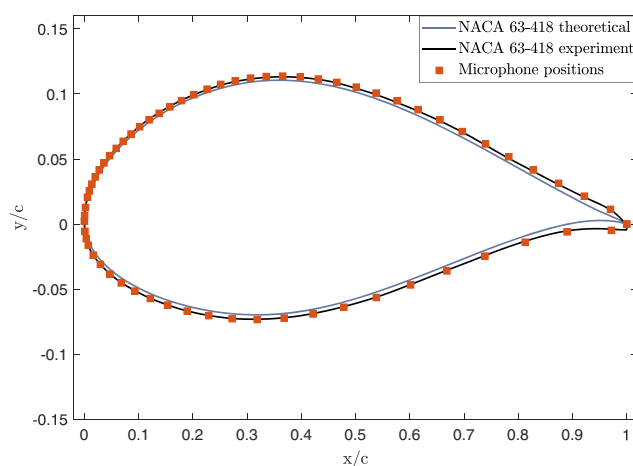


FIGURE 1 NACA 63-418 theoretical and experimental airfoil profiles with microphone placements [Colour figure can be viewed at wileyonlinelibrary.com]

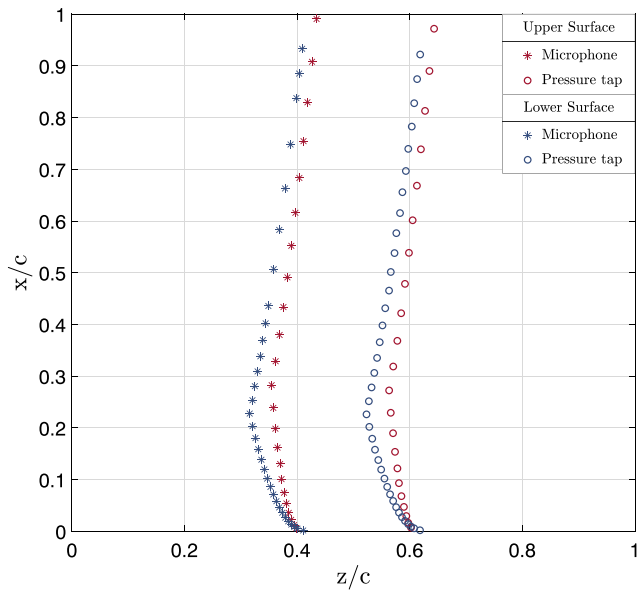


FIGURE 2 Spanwise distribution of the microphones and pressure taps on the lower and the upper surfaces [Colour figure can be viewed at wileyonlinelibrary.com]

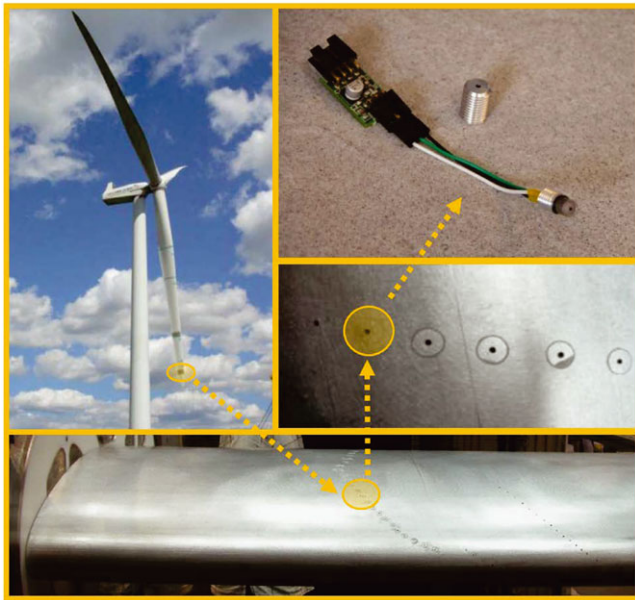


FIGURE 3 NM-80 wind turbine, surface flush-mounted microphones, and 2-D model in the wind tunnel [Colour figure can be viewed at wileyonlinelibrary.com]

Transition is highly affected by the pressure gradients, therefore in addition to the surface microphones, surface pressure measurements were also conducted simultaneously by the pressure holes placed at a slightly different spanwise position on the same model at both suction and pressure sides. Therefore, in addition to the pressure fluctuations measured by high-frequency response microphones, the pressure coefficient (C_p) distributions on the surface are obtained by processing the data from the pressure taps. The pressure tap data is acquired at 5 Hz for 50 seconds.

The experiments were conducted at the LM Glasfiber Low Speed Wind Tunnel, which has a test section width of 1.35 m, a height of 2.70 m, and a length of 7 m.²¹ The turbulence intensity (T.I.; root mean square of the velocity fluctuations divided by the mean velocity) of the LM wind tunnel is around 0.1 % which plays an important role for the inflow conditions and for choosing the amplification factor (N) for the numerical calculations.

The estimation of the N_{tr} (the amplification factor at transition) by the envelope method may result in a slightly less value than the one calculated by the e^N method.²² Therefore, several N_{tr} values (4, 5, 6, 7, 8, and 9, which corresponds to T.I. values of 0.563%, 0.371%, 0.245%, 0.161%, 0.106%, and 0.070%, respectively) are chosen for comparison. Mack's relation²³ in Equation 1 is used to relate the T.I. values to the N factors at transition.

$$N_{tr} = -8.43 - 2.4 \cdot \ln(T.I.). \quad (1)$$

Experiments were conducted at the Reynolds numbers (Re) of typical operating conditions of horizontal axis wind turbines ($1.6 \cdot 10^6$, $3 \cdot 10^6$, $4 \cdot 10^6$, $5 \cdot 10^6$, and $6 \cdot 10^6$). The AOA values were varied from -15° to 16° with 1° increments. Furthermore, the increments were decreased by half between -3° to 5° . The data were sampled at 50 000 Hz for 10 seconds for each test case.

3 | EXPERIMENTAL DATA ANALYSIS

The time series of the pressure fluctuations obtained from the microphones are examined by time and frequency analysis of different statistical quantities in order to investigate the transition characteristics of the NACA 63-418 airfoil and establish a robust method for transition detection. Time signals are analysed in the frequency domain by fast Fourier transform (FFT). The power spectra of the pressure fluctuations are calculated by the Welch's²⁴ PSD estimate algorithm of MATLAB. A parametric study is performed for different data segment lengths. The number of discrete Fourier transform (DFT) points (n_{fft}) is selected as 2048. Thus, the window size is 2048, which has a frequency resolution of 24 Hz. Moreover, 50% overlapping is applied. The resultant PSD has a size of $n_{fft}/2 + 1 = 1025$, and it is one-sided and doubled in magnitude. This configuration keeps the peaks and provides smooth spectra.

The spectrogram analyses are also performed by dividing data length (L) into k columns, which is determined by the following equation:

$$k = (L - N_{overlap}) / (W - N_{overlap}). \quad (2)$$

The number of overlapped samples ($N_{overlap}$) for spectrogram analysis is 1024 and the window size (W) is 2048, resulting in $k = 487$ columns. In this way, PSD of each 0.0205 seconds of the 10 seconds data is created for each microphone.

3.1 | Background noise and calibration

Background noise from the wind tunnel was captured by a microphone which was placed outside the tunnel. It can be seen from Figure 4 that the laminar spectra at $x/c = 0.12, 0.32$, and 0.54 exhibit peaks equal to the background noise peaks and their harmonics. These laminar spectra of the pressure fluctuations have a higher magnitude at lower frequencies. On the other hand, turbulent spectra, observed at $x/c = 0.81$ in Figure 4, has a higher magnitude at higher frequencies.

The coherence between the microphone at $x/c = 0.54$ at the pressure side and the background microphone is analysed for $AOA = 6^\circ$ and $Re = 3 \cdot 10^6$ and the results are presented in Figure 5. The magnitude squared coherence (C_{xy}) between these microphones is calculated from the power spectral densities ($P_{xx}(f)$ and $P_{yy}(f)$) and the cross PSD ($P_{xy}(f)$) as follows:

$$C_{xy}(f) = \frac{|P_{xy}(f)|^2}{P_{xx}(f) \cdot P_{yy}(f)}. \quad (3)$$

Here, the x letter denotes the microphone at $x/c = 0.54$ at the pressure side, and the y letter indicates the background microphone. The surface microphone under laminar flow conditions is selected for comparison since the noise peaks are more apparent in this spectra. The wind tunnel main noise peak is observed at 1647.9 Hz. This peak is due to the wind tunnel fan and it moves to higher frequencies as the wind tunnel velocity is increased due to the increased rotational speed of the fan. This can be seen from the PSD for Reynolds numbers from 1.6 to 6 million for $x/c = 0.54$ at $AOA = 6^\circ$ in Figure 6. Moreover, it is observed that for the $AOAs$ higher than 12° , a peak appears in the spectra as a result of the stall conditions. At the stall conditions, energy in the low-frequency region increases due to the irregularities in the flow and vortices.

The microphone with the flushing adaptor house design is chosen for minimizing surface disturbances and the measurement area. The final installed microphones on the model were not calibrated individually. However, a comprehensive calibration, investigating different parameters, was done by Brüel and Kjær (B & K) on three randomly picked microphones installed in the same type of adaptors. The measurement error plots

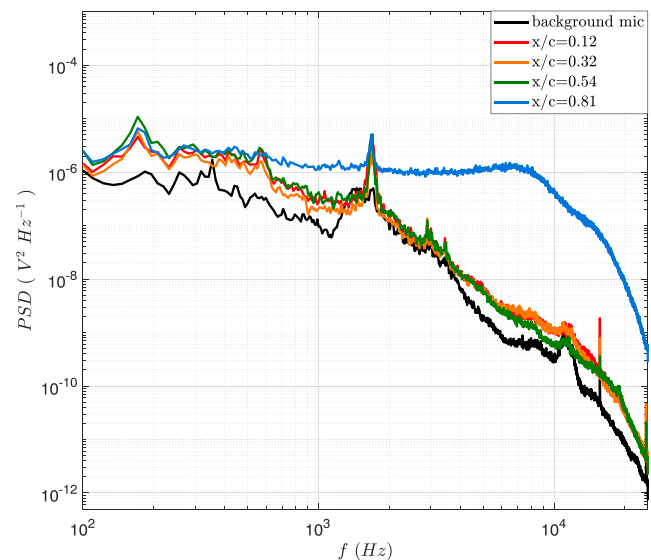


FIGURE 4 Spectra of the selected chordwise positions on the lower surface and of the background microphone, $Re = 3 \cdot 10^6$ at $AOA = 6^\circ$ [Colour figure can be viewed at [wileyonlinelibrary.com](https://onlinelibrary.wiley.com)]

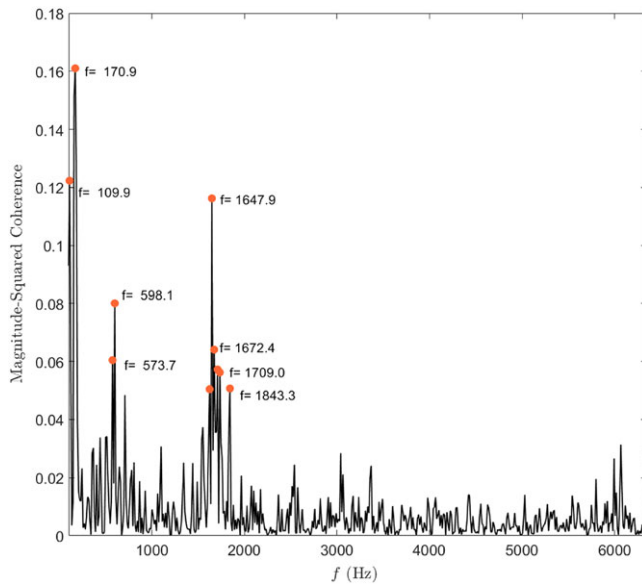


FIGURE 5 Coherence analysis for the microphone at $x/c = 0.54$ on lower surface, $Re = 3 \cdot 10^6$, $AOA = 6^\circ$ [Colour figure can be viewed at wileyonlinelibrary.com]

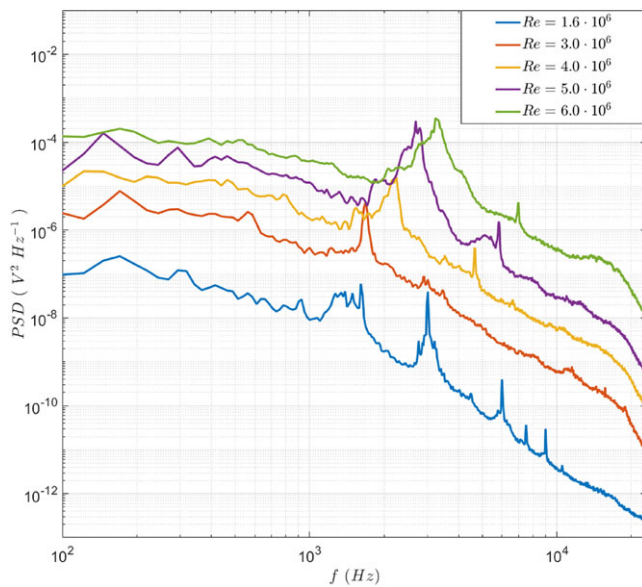


FIGURE 6 PSD at $x/c = 0.54$ on lower surface at $AOA = 6^\circ$ for various Reynolds Numbers [Colour figure can be viewed at wileyonlinelibrary.com]

indicate an amplification peak of around 4 dB just above 10 kHz, where around half of this amplification is due to the flushing adaptor. Another important result was that the deviation between three randomly picked microphones, and each one of them mounted, measured, and dismantled three times showed a maximum deviation in an amplitude of less than 1 dB below 10 kHz. Therefore, a flat response is assumed and a default value of the sensitivity at 1000 Hz provided by the manufacturer is used to convert voltage signals to pressure (Pa).

3.2 | Transition detection methods

The time signal and PSD of the data can indicate when the flow becomes turbulent. However, analysing these signals is not an automated process. In order to obtain an autonomous method, a transition detection algorithm is generated by applying two methods, namely standard deviation and the first moment of the spectra. In both methods, an interpolation is performed to determine more explicitly the location for laminar to turbulent boundary layer transition.

3.2.1 | Standard deviation

In order to calculate the root mean square (RMS) from the frequency domain, Equations 4 and 5 are used. The effect of the integration frequency limits on detection of the transition location is analysed. Looking at the laminar and the turbulent spectra at Figure 4, it is seen that the maximum observable difference in magnitudes are in the range of 2 kHz to 10 kHz. For the frequencies higher than 7000 Hz, a bump in the turbulent spectra is observed due to the resonance in the tubing system caused by the pinhole placement of the microphones. Thus, frequencies higher than 7000 Hz are excluded. Frequencies lower than 2000 Hz are also eliminated, where the effect of inflow turbulence and large eddies in stall are dominant. Moreover, a parametric study on detected transition points for various integrated frequency intervals is performed. As a result

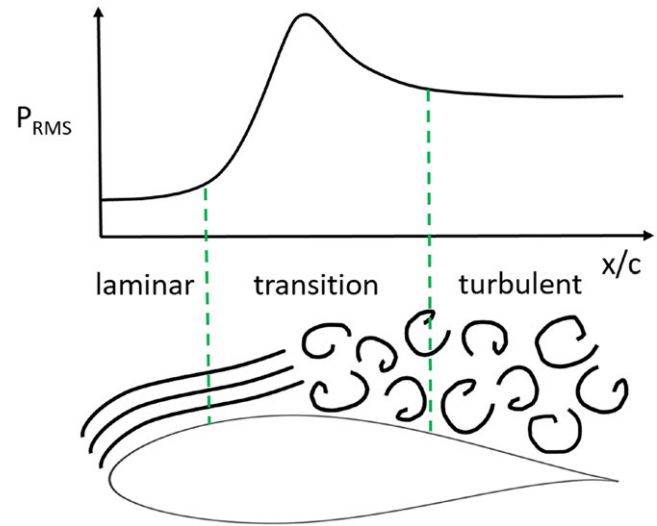


FIGURE 7 Chordwise pressure fluctuation changes during laminar to turbulent boundary layer transition [Colour figure can be viewed at wileyonlinelibrary.com]

of this parametric study and considering the observable region of the spectra and the microphone signal properties, the frequency range of $f_1 = 2000$ Hz to $f_2 = 7000$ Hz is found to be the best range for analysing the transition location.

$$P_{RMS}^2 = \int_{f_1}^{f_2} PSD df. \quad (4)$$

$$\sigma = \sqrt{P_{rms}^2}. \quad (5)$$

Here, the σ (standard deviation) is considered as the total energy of the pressure fluctuations within a certain frequency range specified by the integration boundaries. It should be noted that the PSD generated is already doubled in magnitude and one sided. The RMS is expressed in terms of decibels (dB) by Equation 6, taking the reference pressure as $P_{ref} = 20 \mu$ Pa as follows:

$$L_p = 20 \cdot \log_{10} \left(\frac{P_{rms}}{P_{ref}} \right). \quad (6)$$

As the transition is in process, an increase of pressure fluctuations with a peak is expected, ending up at a higher level of fluctuations when the flow becomes fully turbulent as illustrated in Figure 7. Therefore, in the current method, a sudden chordwise increase in the L_p is considered as an indication of the transition location. The transition detection is performed by first interpolating the chordwise L_p and taking its moving average. Then, the transition point is determined by the highest first derivative as in Equation 7 and checking for the zero crossing of the second derivative of the L_p .¹⁸

$$x_{tr} = x \rightarrow \max \left(\frac{dL_p}{dx} \right). \quad (7)$$

3.2.2 | First moment of the spectra

The second transition detection method is based on the first moment of the spectra, which is calculated by Equation 8. It is denoted by f_μ . In this method, the PSD is approached as probability density function by calculating the mean normalized by the probability distribution. The high-frequency content of the spectra, where the transition peaks are expected, is amplified by multiplication by the frequency (f). Large f_μ value indicates that the energy proportion at high frequencies is larger than at low frequencies.

$$f_\mu = \frac{\int_{f_1}^{f_2} f \cdot PSD df}{\int_{f_1}^{f_2} PSD df}. \quad (8)$$

According to the moment method, maximum positive derivative of f_μ with respect to chordwise position gives the transition location for each AOA value as shown in Equation 9 as follows:

$$x_{tr} = x \rightarrow \max \left(\frac{df_\mu}{dx} \right). \quad (9)$$

This transition detection method was validated for different airfoils by Døssing²⁵ and for NACA 63-418 airfoil with surface roughness elements (zigzag tape) by Özçakmak et al.²⁶

Both the Lp derivative method and the spectral moment method are applied to the interpolated data with 100 points. The frequency range is selected as the same as for the standard deviation method. In both of the transition detection methods, a sudden increase in the moment and standard deviation is traced with the condition that the increased values maintain at that level. The steps for transition detection can be summarized as follows:

- Increase the resolution by interpolating the microphone positions.
- At a chosen AOA and Reynolds number, sort Lp or f_μ in the chordwise direction.
- Detect the highest derivative of Lp or f_μ provided that the increased derivative level maintains and transition position propagates chordwise.
- Check the zero crossing of the second derivative.

3.3 | Uncertainty and accuracy of the measurements

The airfoil section is a direct copy of the geometry of the full-scale blade, which is already influenced by the installation of the microphones. Therefore, the model is manufactured with same surface shape deviations and microphone placement as used on the 3-D blade and limitations due to postinstallation. This might be one of the reasons for the suction side transition behaviour at the particular AOA values. In addition, the placement and the number of the microphones may cause interaction resulting in downstream microphones being in the wake of upstream ones. Since the upper surface has a bigger curvature than the lower surface, surface mounting may result in cavities around microphones if not carefully handled. These cavities may introduce instabilities to the flow resulting in an earlier transition. Therefore, microphones should be placed spanwise with a wider angle than the turbulence wedge angle caused by the existence of the microphone itself. The distance between the neighbouring microphones is added to the results as the error bars of the measurements. The distance between microphones would be more a significant source of inaccuracy if only the standard deviation peaks were investigated. However, by the moment and Lp derivative approaches, this inaccuracy is highly eliminated by the interpolation.

4 | RESULTS AND DISCUSSION

4.1 | Time series analysis

The time signals of the microphones on both suction and pressure sides for various AOA values are presented at Figures 8 and 9, respectively, for $Re = 3 \cdot 10^6$. The time segment from 4.4 to 4.8 seconds is selected in order to present the signal in detail. The signals are uniform in time due to low T.I. of the wind tunnel, therefore any time segment would indicate a similar behavior. The signals, where the amplitude of the pressure fluctuations is low, indicates laminar boundary layer. Transitional flow can be observed with high-amplitude, high-frequency fluctuations followed by a decrease in magnitude when it becomes fully turbulent, the value though still remains higher than the laminar fluctuations. For instance, in Figure 8B, at $AOA = -6^\circ$, transition is in process from $x/c = 0.62$ to $x/c = 0.66$ on the suction side. At $AOA = 0^\circ$ on the suction side (Figure 8C), different behaviour is observed. In this case, at $x/c = 0.31$, the time series indicate a turbulent signal just after the laminar signal at $x/c = 0.25$ due to a possible microphone-flow interaction and surface irregularity, which is explained in detail at Section 4.3. Moreover, at $AOA = 12^\circ$,

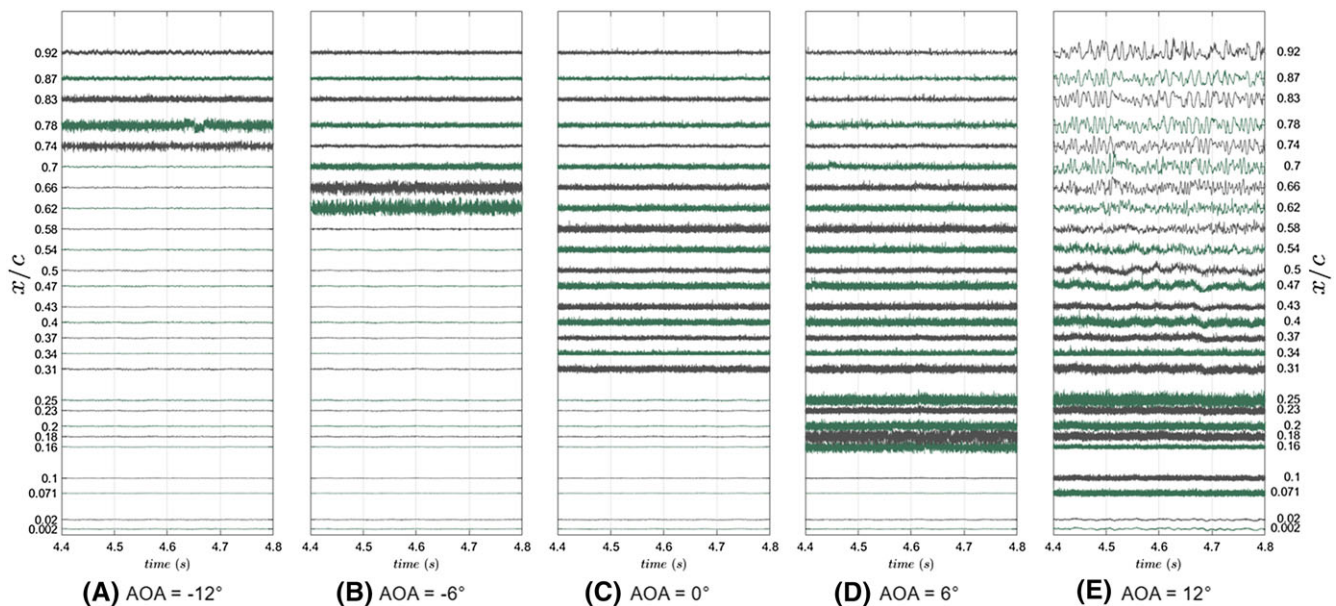


FIGURE 8 Time signals from microphones at different chordwise locations on the suction side at $Re = 3 \cdot 10^6$ [Colour figure can be viewed at wileyonlinelibrary.com]

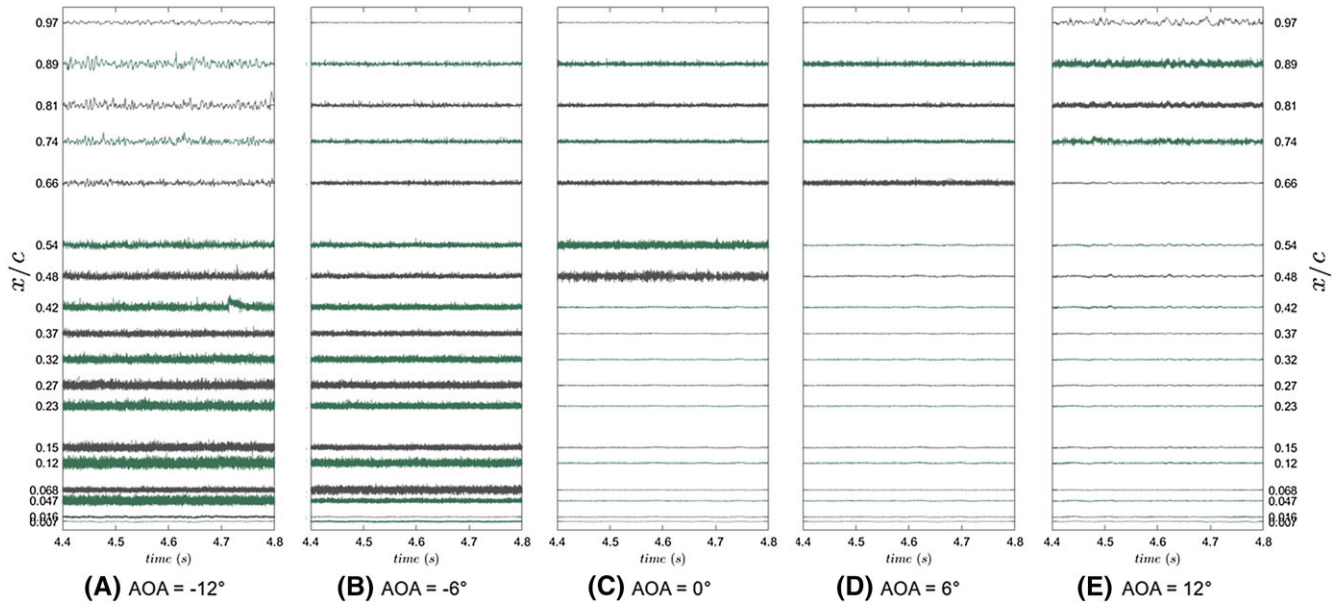


FIGURE 9 Time signals from microphones at different chordwise locations on the pressure side at $Re = 3 \cdot 10^6$ [Colour figure can be viewed at wileyonlinelibrary.com]

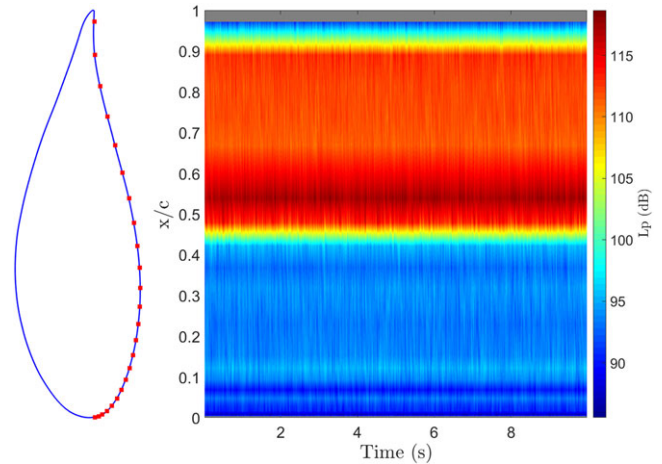


FIGURE 10 Pressure level (L_p) spectrogram along the pressure side at $Re = 3 \cdot 10^6$ at angle of attack (AOA) = 0° [Colour figure can be viewed at wileyonlinelibrary.com]

at Figure 8E, the signals indicate a transition to turbulent flow and at further downstream, the low-frequency high-amplitude signal indicates turbulent separation. It should be noted that, for the approximated NACA 63-418 airfoil used in the experiments, the stall AOA at $Re = 3 \cdot 10^6$ is 11.7° .¹⁸

4.2 | Transition locations from L_p and f_m

A sudden chordwise increase of the L_p indicates a laminar to turbulent transition on the airfoil. The spectrogram of the pressure side at the 0° AOA at a Reynolds number of $3 \cdot 10^6$ can be seen in Figure 10. There is a significant increase in the L_p at $x/c = 0.45$, which indicates a transition to turbulent flow. From the spectrogram, it is also observed that the data is constant in time due to the low T.I. of the wind tunnel.

The L_p method is applied for a various AOA values. The detected transition locations are presented in Figure 11. The error bars indicate the distance to the neighbouring microphones. The detected points are at the locations of highest chordwise increase of pressure dB levels.

The chordwise L_p for various AOA values at $Re = 3 \cdot 10^6$ on pressure side is presented in Figure 12. The regions of laminar, transitional, and turbulent flow are highlighted.

When there is a natural transition, a peak appears during the transition process and it is always higher than turbulent pressure levels. When the flow becomes turbulent, the pressure level remains almost at a constant value. In some cases on the suction side, this peak is not observed when there is a sudden transition to turbulent flow due to the surface irregularities or microphone placement.

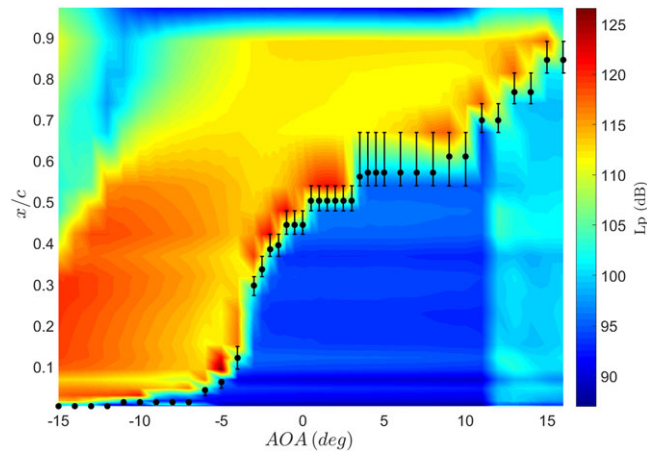


FIGURE 11 Pressure levels (L_p) for various angle of attack (AOA) values with transition points detected from the increase in the L_p derivative for the lower surface [Colour figure can be viewed at wileyonlinelibrary.com]

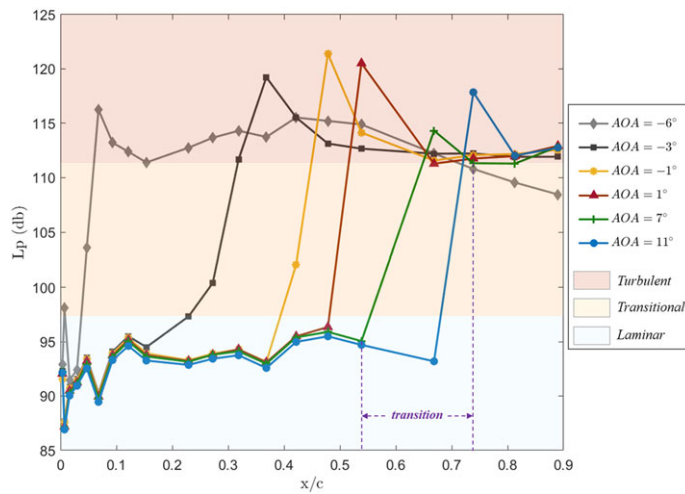


FIGURE 12 Chordwise pressure levels (L_p) for various angle of attack (AOA) values on the pressure side, at $Re = 3 \cdot 10^6$. (Note that the turbulent flow starts when the L_p levels reach to a constant value. Therefore, the peaks seen in the turbulent region belongs to the transitional flow.) [Colour figure can be viewed at wileyonlinelibrary.com]

Flow Condition	$Re = 1.6 \cdot 10^6$	$Re = 3 \cdot 10^6$	$Re = 4 \cdot 10^6$	$Re = 5 \cdot 10^6$	$Re = 6 \cdot 10^6$
Laminar	70-82 dB	85-97 dB	102-108 dB	107-118 dB	112-120 dB
Transitional	83-112 dB	100-123 dB	108-125 dB	118-128 dB	115-134 dB
Turbulent	105-110 dB	112-120 dB	115-120 dB	120-125 dB	123-130 dB

TABLE 1 Pressure dB levels for various Reynolds numbers

Abbreviation: dB, decibel.

The chordwise distance over which the transition takes place is illustrated by the region labeled "transition" as an example for one of the AOA cases at $Re = 3 \cdot 10^6$ in Figure 12. The resolution of the points at laminar, transitional, and turbulent flow differs in each case. However, by analysing the data at all Reynolds numbers and AOA values, a common conclusion is reached. It is found that the curve length from the initiation of the transition process to fully turbulent flow can vary between 0% to 30% and is most commonly around 15% to 20 %. The vertical coloring in Figure 12 indicates the classification of the flow: whether it is laminar, transitional, or turbulent.

Moreover, the dB levels are identified for laminar, transitional, and turbulent flow at all Reynolds numbers and presented in Table 1. The dB levels increase with Reynolds number as well as depending on the wind tunnel noise.

The transition positions detected by the moment method are presented with f_μ contours in Figure 13. The transition locations are detected at the maximum derivative of f_μ . It can be seen from the figure that these locations correspond to where contour lines get closer, indicating a high derivative. Furthermore, the width of the band indicates the length of the chordwise distance that the transition occurs.

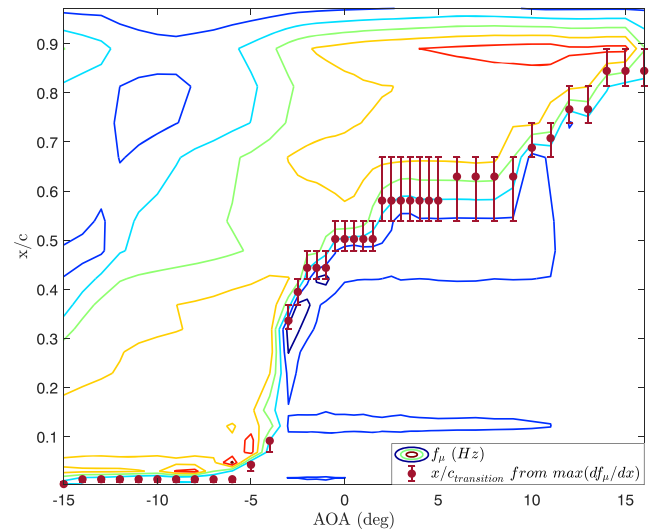


FIGURE 13 f_m contours and detected transition locations vs angle of attack at the pressure side at $Re = 3 \cdot 10^6$ [Colour figure can be viewed at wileyonlinelibrary.com]

4.3 | Transition detection methods in comparison with numerical computations

The detected transition points for each of AOA for both suction and pressure sides are given in Figure 14. The XFOIL²⁷ calculations are performed for different N numbers of 4, 5, 6, 7, 8, and 9 based on the experimental airfoil contour. The DTU in-house computational fluid dynamics (CFD) EllipSys code²⁸ computations are performed at $N = 8$. Transition to turbulence in EllipSys code is governed by the semi-empirical e^N model. The shape factor and the momentum thickness are found from the solution of the von Karman boundary layer equations, beginning at the stagnation line and integrating downstream until the transition location is found. During the integration of the boundary layer equations, a check is carried out to detect whether disturbances are amplified or damped. When solving the Navier-Stokes equations, transition to turbulence is handled by the intermittency factor that controls the effective viscosity. The intermittency factor is 0 at the laminar flow and gradually increases to 1 after transition.

The EllipSys code predicts the transition location slightly upstream compared to XFOIL predictions due to the implementation differences. On the pressure side, EllipSys- and XFOIL-predicted transition locations are in agreement with the measured ones or they are within the error bars. However, on the suction side, instead of a gradual change of the transition location with AOA, the transition location suddenly moves to 27% chord at -5° in the experimental data. From -5° to 5° , the experimental data differs from the XFOIL and EllipSys results due to an experimental issue, which will be explained shortly after. That nonfitting region on the suction side is marked with a blue color in Figure 14A.

The pressure tap measurements are also analysed to compare with the microphone results. In addition to the XFOIL computations, EllipSys computations are used to predict pressure distributions of the experimental airfoil contour. The experimental C_p values, Xfoil, and EllipSys calculations are presented in Figure 15. The C_p distribution results show a good agreement. At $AOA=0^\circ$ at $x/c=0.52$ on the suction side, sudden change of the slope is observed from both the numerical and the experimental results. Transition location results from the XFOIL in Figure 14A also indicates the same location as expected. However, the experimental results indicate the transition at $x/c=0.27$ on the suction side. Therefore, the sudden jump of the transition point to 27% from -6° to -5° is found not to be the result of natural transition. Adverse pressure gradients on the surface and surface irregularities in combination with the microphone placement (upstream microphones and their wake) and the cavity around certain microphones might cause a turbulent wedge that effects all the downstream microphones. The C_p plots of experiments, EllipSys and Xfoil, and predicted transition locations by XFOIL show that the natural transition is happening much further downstream. A bump around $x/c=0.27$ can be observed at C_p distributions from the results of XFOIL, EllipSys, and experiments in Figure 15. However, small irregularities can not be perceived by e^N envelope method in XFOIL with the current amplification ratio for the wind tunnel T.I. Therefore, even though the bumps in the C_p graphs from XFOIL are visible, the transition prediction in XFOIL can not account for these surface irregularities.

In order to verify that the chordwise increase in Lps is a result of boundary layer transition, the amplification of the initial instabilities of the T-S waves are analysed. The initial disturbance amplitude A_0 of the pressure spectra at the leading edge amplifies and the amplification ratio can be expressed by an exponential function e^N . The transition location can be determined by calculating the amplification ratio (N) reaching a certain value.²⁹ Therefore, the N factor is calculated by Equation 10 as follows:

$$N = \ln \left(\frac{A}{A_0} \right). \quad (10)$$

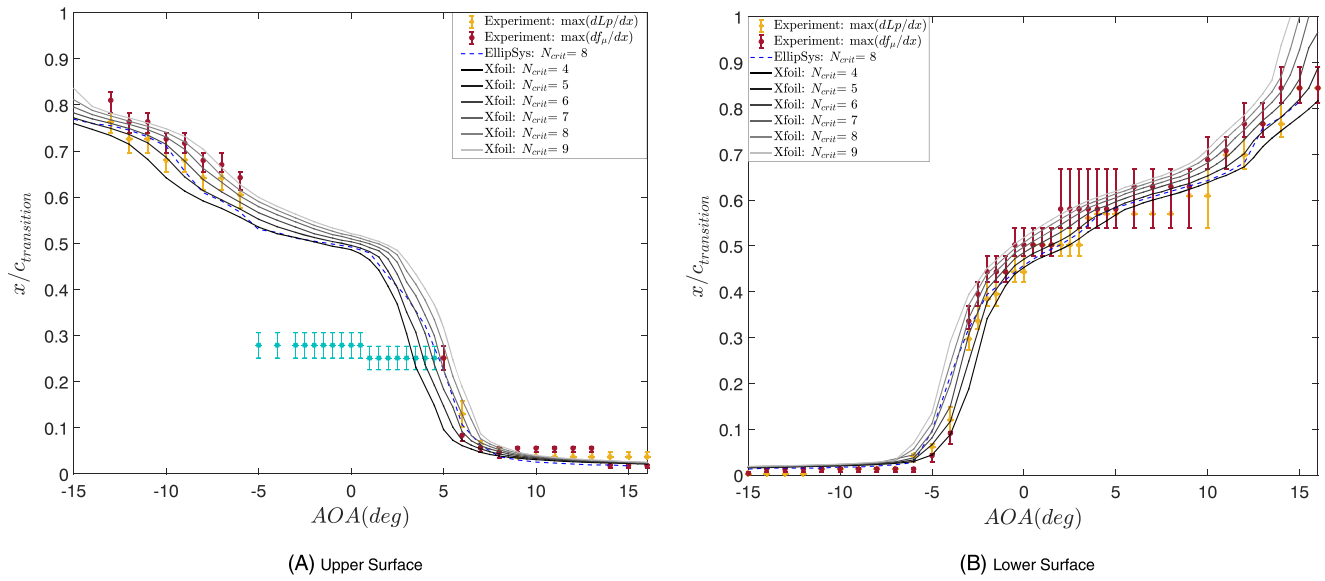


FIGURE 14 XFOIL and EllipSys comparisons with experimentally detected transition locations for all angles of attack at $Re = 3 \cdot 10^6$ [Colour figure can be viewed at wileyonlinelibrary.com]

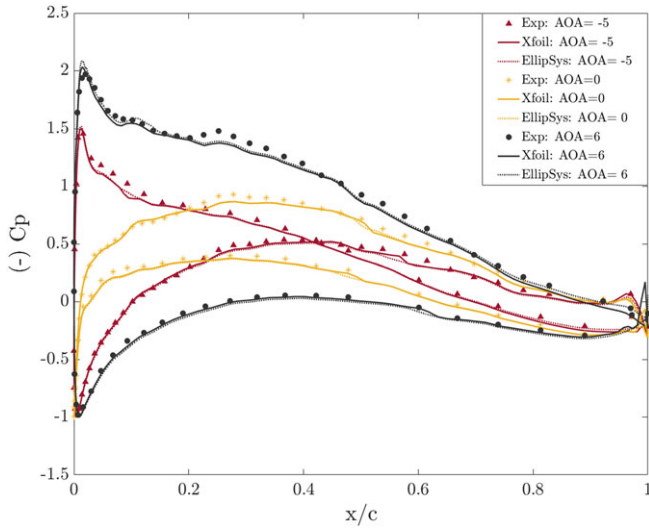


FIGURE 15 C_p distributions from experiments, Xfoil and EllipSys computations at $Re = 3 \cdot 10^6$ [Colour figure can be viewed at wileyonlinelibrary.com]

The N factor defines the growth of disturbances and must be evaluated for various frequencies.³⁰ Laminar to turbulent transition occurs where N factor has a sudden chordwise increase. The N growth is shown for various frequencies for the pressure side at $AOA=0^\circ$ at $Re = 3 \cdot 10^6$ in Figure 16. It can be seen that the amplification ratio of the initial disturbances gets maximum around the position of the detected transition point.

4.4 | T-S frequencies and the neutral curve

Using the experimentally detected transition locations at each AOA and Reynolds number, the corresponding boundary layer location is inspected in XFOIL computations in order to estimate the displacement thickness (δ^*). Based on this, the Reynolds number based on displacement thickness (Re_{δ^*}) is calculated from Equation 11. U_e is the edge velocity and ν denotes the kinematic viscosity of the air.

$$Re_{\delta^*} = \frac{U_e \cdot \delta^*}{\nu}. \quad (11)$$

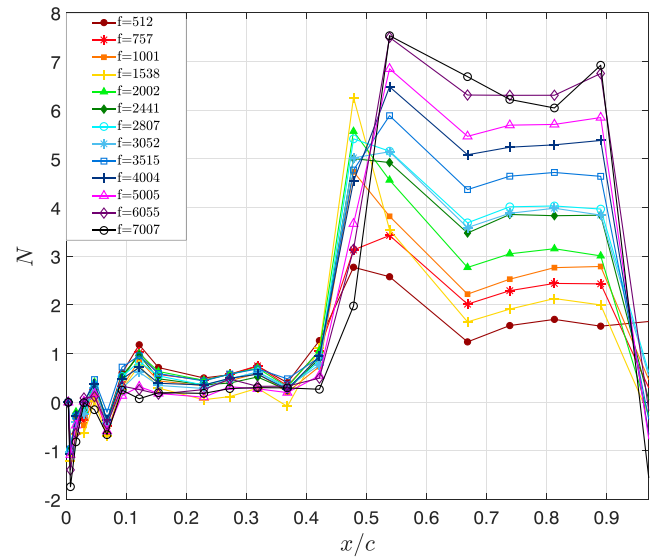


FIGURE 16 N factor vs chord positions on the pressure side at $Re = 3 \cdot 10^6$, at angle of attack (AOA) = 0° [Colour figure can be viewed at wileyonlinelibrary.com]

The T-S frequencies (f_{TS}) at each Reynolds number and AOAs are determined by analyzing the absolute value of the Fourier coefficients. For this purpose, the power of the signal at each frequency is analysed, and the initial disturbance bumps that grows from laminar to turbulent spectra are observed. This is illustrated in Figure 17 that is obtained at $Re = 5 \cdot 10^6$ at AOA = -2.5° . The two dark gray lines indicate laminar spectra at $x/c = 1.16\%$ and 12.16% . Moreover, the lighter two gray lines are for the turbulent spectra at $x/c = 36.83\%$ and 42.17% . The region in between shows the transitional growth. A bump in the spectra appears at $x/c = 15.37\%$ at $f_{TS} = 5811$ Hz. This T-S bump grows in amplitude further downstream with a shift to lower frequencies into a broadband region.

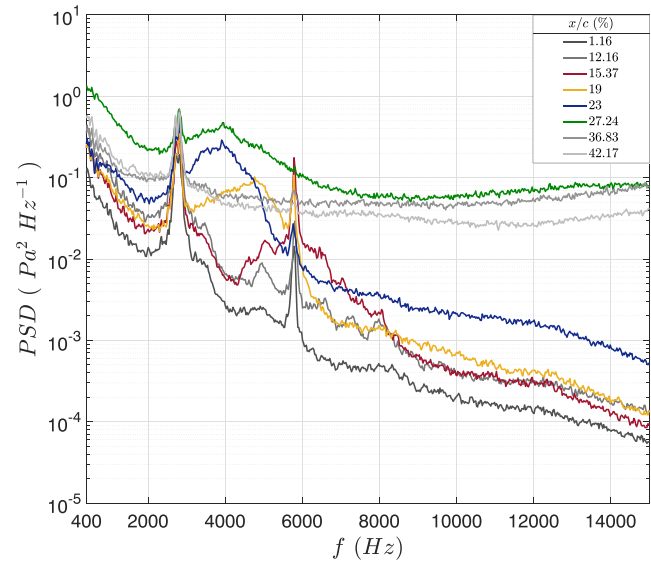


FIGURE 17 Power spectral density (PSD) at $Re = 5 \cdot 10^6$, at angle of attack (AOA) = -2.5° [Colour figure can be viewed at wileyonlinelibrary.com]

The nondimensional frequency³¹ is calculated from Equation 12 with the T-S frequencies (f_{TS}) obtained from the experiments and the edge velocities (U_e) from the XFOIL computations.

$$F = \frac{2 \cdot \pi \cdot f_{TS} \cdot \nu}{U_e^2} \cdot 10^6. \quad (12)$$

Figure 18 shows the observed T-S wave frequencies at each AOA for various Re numbers on the pressure side. It is seen that the T-S frequencies are in the range of 1000 to 10 000 Hz for given Reynolds numbers and AOA. The boundary layer on the pressure side becomes more stable as the AOA increases due to favourable pressure gradients. Therefore, as the AOA increases, higher Reynolds numbers are needed to reach the same level of T-S frequency. The opposite behaviour with AOA is expected for the suction side.

Figure 19 shows the nondimensional plot for NACA 63-418 airfoil at corresponding Reynolds numbers. Compared with the neutral curves for the flat plate boundary layer from the previous studies,^{32,33} a higher magnitude of F and wider range of Re_{δ^*} is observed. The closest case to the flat plate theoretical curves is observed to be at $Re = 6 \cdot 10^6$ having a maximum difference of 18%.

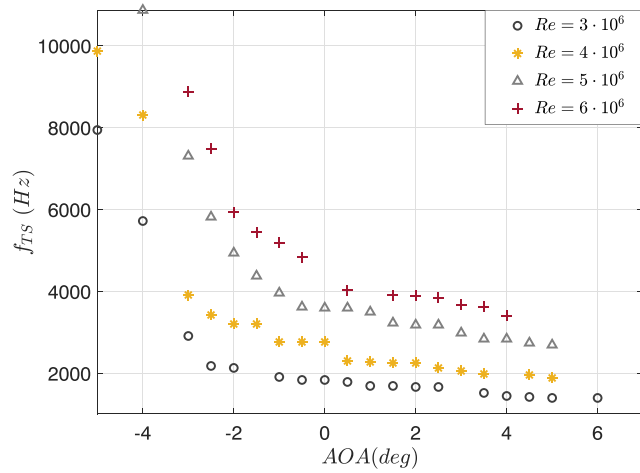


FIGURE 18 Tollmien-Schlichting frequencies [Colour figure can be viewed at wileyonlinelibrary.com]

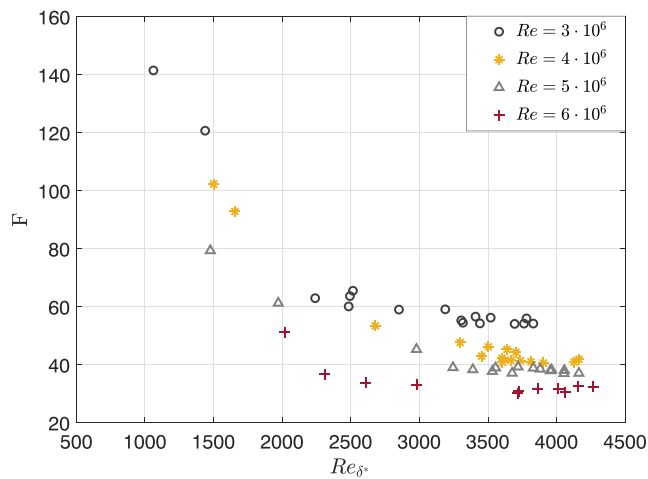


FIGURE 19 F with displacement thickness Re number [Colour figure can be viewed at wileyonlinelibrary.com]

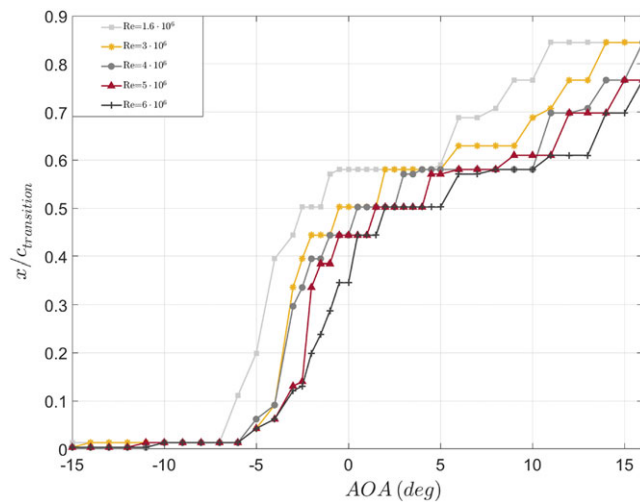


FIGURE 20 Detected transition locations vs angle of attack at the pressure side for various Reynolds numbers [Colour figure can be viewed at wileyonlinelibrary.com]

4.5 | Reynolds number dependency of the transition location

The detected transition locations on the pressure side are presented at Figure 20. The Reynolds number dependency is clearly observed from the figure. As the Reynolds number increases, the transition location moves closer to the leading edge for a given AOA. The suction side is not shown because of the previously discussed behaviour in the middle AOA range. However, in the valid AOA range, there is a consistent behaviour of earlier transition closer to the leading edge as the Reynolds number increases.

5 | CONCLUSION

Accurate detection of laminar to turbulent boundary layer transition location is significant for airfoil design and performance of the wind turbines. Several methods can visualize and show transition location on airfoils; however, an autonomous method is established in this study by high-frequency flush-mounted microphone measurements.

Time series of the pressure fluctuations are analysed in time and frequency domain for NACA 63-418 airfoil from the LM 38.8 blade of the NM80 wind turbine. Lp and the moment of the pressure spectra methods are used in order to detect transition for various Reynolds numbers and AOA values. The chordwise increase of Lps and the first moment of the spectra indicates a transition in progress.

The spectrogram analysis is performed to ensure that no time variations exist for the 10 seconds data by the virtue of low T.I. When the wind tunnel T.I. is low, turbulent spectra have higher energy on higher frequencies, resulting in a higher mean value. Therefore, the moment method is found to be more robust to detect transition than the standard deviation method. This method is free of gain errors of the microphones and can be applied when there are fewer microphones installed together with an interpolation. It is seen that, in order to reduce the interaction, the placement and number of the microphones, and possible cavity occurrence during installation on curved surfaces, should be carefully handled, especially on the suction side where there is a higher surface curvature.

A close agreement is found between XFOIL, EllipSys, and the experimental results on the pressure side where there is a natural transition. As the Reynolds number increases from 1.6 to 6 million, the transition point moves forward closer to the leading edge at all AOAs at both suction and pressure sides. At a specific chordwise position, the transition occurs at a lower AOA value for the suction side and at a higher AOA for the pressure side with increasing Reynolds number.

The T-S frequencies are determined from the spectra for various Reynolds numbers and AOAs. As the AOA increases, the boundary layer on the pressure side requires higher Reynolds numbers to have same amplified T-S frequencies. By identification of these frequencies, the data for the neutral curve of the NACA 63-418 airfoil are generated.

It is seen that transition occurs over a substantial part of the chord up to 30%, and typically around 15% to 20% of the chord length. The Lps increase with a peak during the transition process and further decreases when the flow is fully turbulent, being always higher than the laminar dB levels. The Lp dB ranges are identified for laminar, transitional and turbulent flow for all Reynolds numbers.

Considering that the transitional flow can occupy a high percentage of the chord, it is important to have an accurate transition model in numerical tools. In order to develop numerical transition prediction tools, the current database for the NACA 63-418 airfoil with transition locations, T-S frequencies, and N growth values for several frequencies can be used. Furthermore, the current experimental transition detection methods can be applied to new experiments with high-frequency microphones to contribute airfoil and wind turbine blades database. By this way, performance, design, and power production of the wind turbines can be estimated more accurately.

ORCID

Özge Sinem Özçakmak  <https://orcid.org/0000-0001-7884-755X>

Niels Nørmark Sørensen  <https://orcid.org/0000-0002-7185-7429>

Helge Aagaard Madsen  <https://orcid.org/0000-0002-4647-3706>

Jens Nørkær Sørensen  <https://orcid.org/0000-0002-1974-2675>

REFERENCES

1. Bæk P, Fuglsang P. Experimental detection of transition on wind turbine airfoils. In: Proceedings of the European Wind Energy Conference and Exhibition; 2009; Orlando, Florida:1628-1652.
2. Schaffarczyk AP, Schwab D, Breuer M. Experimental detection of laminar-turbulent transition on a rotating wind turbine blade in the free atmosphere. *Wind Energy*. 2017;20(2):211-220.
3. Reshotko E. Boundary-layer stability and transition. *Annu Rev Fluid Mech*. 1976;8(1):311-349.
4. Arnal D, Casalis G. Laminar-turbulent transition prediction in three dimensional flows. *Prog Aerosp Sci*. 2000;36:173-191.
5. Arnal D, Gasparian G, Salinas H. Recent advances in theoretical methods for laminar-turbulent transition prediction. In: 36th AIAA Aerospace Sciences Meeting and Exhibit. Reno, NV; 1998:223.
6. Reed HL, Saric W. Stability of three-dimensional boundary layers. *J Comput Phys*. 1989;21:235-284.
7. Schlichting H, Gersten K. *Boundary Layer Theory*. Berlin: Springer; 2016.
8. Henningson D, Lundblad A, Johansson A. A mechanism for bypass transition from localized disturbances in wall-bounded shear flows. *J Fluid Mech*. 1993;250:169-207.
9. Corke TC, Bar-Sever A, Morkovin MV. Experiments on transition enhancement by distributed roughness. *Phys Fluids*. 1986;29(10):3199-3213.
10. Morkovin MV. Bypass transition to turbulence and research desiderata. In: NASA Lewis Research Center Transition in Turbines. Chicago; 1985:161-204.
11. Gardner A, Richter K. Boundary layer transition determination for periodic and static flows using phase-averaged pressure data. *Exp Fluids*. 2015;56(119):13.
12. Haghir AA, Fallahpour N, Mani M, Tadjfar M. Experimental study of boundary layer in compressible flow using hot film sensors through statistical and qualitative methods. *J Mech Sci Technol*. 2015;29(11):4671-4679.
13. Lorber PF, Carta FO. Unsteady transition measurements on a pitching three-dimensional wing. In: The Fifth Symposium on Numerical and Physical Aspects of Aerodynamic Flows; 1992; Long Beach, CA.

14. Khalid M. The use of hot-film technique for boundary layer studies on a 21% thick airfoil. No. NAE-AN-45, National Aeronautical Establishment. Ottawa; 1987.
15. Crawford BK, Duncan Jr. GT, West DE, Saric WS. Laminar-turbulent boundary layer transition imaging using ir thermography. *Opt Photon J*. 2013;3:233-239.
16. Raffel M, Merz C, Schwermer T, Richter K. Differential infrared thermography for boundary layer transition detection on pitching rotor blade models. *Exp Fluids*. 2015;56(2):30.
17. Madsen HA, Bak C, Paulsen US, et al. The danaero mw experiments. No. Risø-R-1726(EN), Danmarks Tekniske Universitet, Risø Nationallaboratoriet for Bæredygtig Energi. Roskilde; 2010.
18. Trolborg N, Bak C, Aagaard Madsen H, Skrzypinski WR. Danaero mw: Final report. No. 0027(EN), DTU Wind Energy. Roskilde; 2013.
19. Madsen HA, Fuglsang P, Romblad J, et al. The dan-aero mw experiments. In: 48th AIAA Aerospace Sciences Meeting Including the New Horizons Forum and Aerospace Exposition; 2010; Orlando, Florida.
20. Timmer WA. An overview of NACA 6-digit airfoil series characteristics with reference to airfoils for large wind turbine blades. In: 47th AIAA Aerospace Sciences Meeting Including the New Horizons Forum and Aerospace Exposition; 2009; Orlando, Florida.
21. Bertagnolio F. NACA0015 measurements in 1m wind tunnel and turbulence generated noise. No. Risø-R-1657(EN), Technical University of Denmark Roskilde Risø. Roskilde; 2008.
22. Weiss A, Gardner AD, Schwermer T, Klein C, Raffel M. On the effect of rotational forces on rotor blade boundary-layer transition. *AIAA J*. 2018;57(1):252-266.
23. Mack LM. Transition and laminar instability. NASA-CP-153203, California, NASA Jet Propulsion Laboratory; 1977.
24. Welch P. The use of fast Fourier transform for the estimation of power spectra: a method based on time averaging over short, modified periodograms. *IEEE Trans Audio Electroacoust*. 1967;15(2):70-73.
25. Døssing M. High frequency microphone measurements for transition detection on airfoils. Risø-R No. 1645(EN), Danmarks Tekniske Universitet, Risø Nationallaboratoriet for Bæredygtig Energi. Roskilde; 2008.
26. Özçakmak ÖS, Madsen HA, Sørensen N, Sørensen JN, Fischer A, Bak C. Inflow turbulence and leading edge roughness effects on laminar-turbulent transition on NACA 63-418 airfoil. In: Journal of Physics: Conference Series (Online); 2018; Milano, Italy; IOP Publishing:022005.
27. Drela M, Giles M. B. Viscous-inviscid analysis of transonic and low Reynolds number airfoils. *AIAA J*. 1987;25(10):1347-1355.
28. Sørensen NN. General purpose flow solver applied to flow over hills. *Ph.D. Thesis*: Risø National Laboratory; 1995.
29. Van Ingen JL. A suggested semi-empirical method for the calculation of the boundary layer transition region. No. V.T.H.-74, Delft University of Technology. Delft; 1956.
30. Horstmann KH, Quast A, Redeker G. Flight and wind tunnel investigations on boundary layer transition. *J Aircr*. 1990;27(2):146-150.
31. Dini P, Selig MS, Maughmer MD. Simplified linear stability transition prediction method for separated boundary layers. *AIAA J*. 1992;30(8):1953-1961.
32. White FM, Corfield I. *Viscous Fluid Flow*, Vol. 3. New York: McGraw-Hill; 2006.
33. Schubauer G. Laminar boundary-layer oscillations and stability of laminar flow. *J Aerosol Sci*. 1947;14(2):69-78.

How to cite this article: Özçakmak ÖS, Sørensen NN, Madsen HA, Sørensen JN. Laminar-turbulent transition detection on airfoils by high-frequency microphone measurements. *Wind Energy*. 2019;1-15. <https://doi.org/10.1002/we.2361>